



**AFRL-RX-WP-JA-2018-0041**

**APPLICATION OF CHARACTERIZATION,  
MODELING, AND ANALYTICS TOWARDS  
UNDERSTANDING PROCESS-STRUCTURE LINKAGES  
IN METALLIC 3D PRINTING (POSTPRINT)**

**M.A. Groeber, E. Schwalbach, S. Donegan, K. Chaput, T. Butler, and J. Miller**

**AFRL/RX**

**27 JULY 2017  
Interim Report**

**Distribution Statement A.  
Approved for public release: distribution unlimited.**

**© 2017 IOP PUBLISHING**

**(STINFO COPY)**

**AIR FORCE RESEARCH LABORATORY  
MATERIALS AND MANUFACTURING DIRECTORATE  
WRIGHT-PATTERSON AIR FORCE BASE, OH 45433-7750  
AIR FORCE MATERIEL COMMAND  
UNITED STATES AIR FORCE**

# REPORT DOCUMENTATION PAGE

*Form Approved*  
OMB No. 0704-0188

The public reporting burden for this collection of information is estimated to average 1 hour per response, including the time for reviewing instructions, searching existing data sources, gathering and maintaining the data needed, and completing and reviewing the collection of information. Send comments regarding this burden estimate or any other aspect of this collection of information, including suggestions for reducing this burden, to Department of Defense, Washington Headquarters Services, Directorate for Information Operations and Reports (0704-0188), 1215 Jefferson Davis Highway, Suite 1204, Arlington, VA 22202-4302. Respondents should be aware that notwithstanding any other provision of law, no person shall be subject to any penalty for failing to comply with a collection of information if it does not display a currently valid OMB control number. **PLEASE DO NOT RETURN YOUR FORM TO THE ABOVE ADDRESS.**

<b>1. REPORT DATE (DD-MM-YY)</b> 27 July 2017		<b>2. REPORT TYPE</b> Interim		<b>3. DATES COVERED (From - To)</b> 19 March 2014 – 27 June 2017	
<b>4. TITLE AND SUBTITLE</b> APPLICATION OF CHARACTERIZATION, MODELING, AND ANALYTICS TOWARDS UNDERSTANDING PROCESS-STRUCTURE LINKAGES IN METALLIC 3D PRINTING (POSTPRINT)				<b>5a. CONTRACT NUMBER</b> IN-HOUSE	
				<b>5b. GRANT NUMBER</b>	
				<b>5c. PROGRAM ELEMENT NUMBER</b>	
<b>6. AUTHOR(S)</b> M.A. Groeber, E. Schwalbach, S. Donegan, K. Chaput, T. Butler and J. Miller – AFRL/RX				<b>5d. PROJECT NUMBER</b>	
				<b>5e. TASK NUMBER</b>	
				<b>5f. WORK UNIT NUMBER</b> X0W6	
<b>7. PERFORMING ORGANIZATION NAME(S) AND ADDRESS(ES)</b> AFRL/RX Wright-Patterson Air Force Base Dayton, OH 45433				<b>8. PERFORMING ORGANIZATION REPORT NUMBER</b>	
<b>9. SPONSORING/MONITORING AGENCY NAME(S) AND ADDRESS(ES)</b>  Air Force Research Laboratory Materials and Manufacturing Directorate Wright-Patterson Air Force Base, OH 45433-7750 Air Force Materiel Command United States Air Force				<b>10. SPONSORING/MONITORING AGENCY ACRONYM(S)</b> AFRL/RXCA	
				<b>11. SPONSORING/MONITORING AGENCY REPORT NUMBER(S)</b> AFRL-RX-WP-JA-2018-0041	
<b>12. DISTRIBUTION/AVAILABILITY STATEMENT</b> Distribution Statement A. Approved for public release: distribution unlimited.					
<b>13. SUPPLEMENTARY NOTES</b> PA Case Number: 88ABW-2017-3509; Clearance Date: 27 Jul 2017. This document contains color. Journal article published in IOP Conference Series: Materials Science and Engineering, Vol. 219, 1 Aug 2017. © 2017 IOP Publishing. The U.S. Government is joint author of the work and has the right to use, modify, reproduce, release, perform, display, or disclose the work. The final publication is available at <a href="http://iopscience.iop.org/article/10.1088/1757-899X/219/1/012002">http://iopscience.iop.org/article/10.1088/1757-899X/219/1/012002</a>					
<b>14. ABSTRACT (Maximum 200 words)</b> This paper presents methods for combining process monitoring, thermal modelling and microstructure characterization together to draw process-to-structure relationships in metal additive manufacturing. The paper discusses heterogeneities in the local processing conditions within additively manufactured components and how they affect the resulting material structure. Methods for registering and fusing disparate data sources are presented, and some effort is made to discuss the utility of different data sources for specific microstructural features of interest. It is the intent that this paper will highlight the need for improved understanding of metallic additive manufacturing processes and show that combining experimental data with modelling and advanced data processing and analytics methods will accelerate that understanding.					
<b>15. SUBJECT TERMS</b> Additive Manufacturing; heterogeneous processing; topology optimization; EOS M280 laser powder-bed fusion					
<b>16. SECURITY CLASSIFICATION OF:</b>			<b>17. LIMITATION OF ABSTRACT:</b> SAR	<b>18. NUMBER OF PAGES</b> 18	<b>19a. NAME OF RESPONSIBLE PERSON (Monitor)</b> Matthew Lesaint <b>19b. TELEPHONE NUMBER (Include Area Code)</b> (937) 255-3636
<b>a. REPORT</b> Unclassified	<b>b. ABSTRACT</b> Unclassified	<b>c. THIS PAGE</b> Unclassified			

# Application of characterization, modelling, and analytics towards understanding process-structure linkages in metallic 3D printing

M A Groeber, E Schwalbach, S Donegan, K Chaput, T Butler and J Miller

Air Force Research Laboratory, Materials and Manufacturing Directorate, 2230 Tenth St., Wright-Patterson AFB, OH 45419

Corresponding Author: michael.groeber@us.af.mil

**Abstract.** This paper presents methods for combining process monitoring, thermal modelling and microstructure characterization together to draw process-to-structure relationships in metal additive manufacturing. The paper discusses heterogeneities in the local processing conditions within additively manufactured components and how they affect the resulting material structure. Methods for registering and fusing disparate data sources are presented, and some effort is made to discuss the utility of different data sources for specific microstructural features of interest. It is the intent that this paper will highlight the need for improved understanding of metallic additive manufacturing processes and show that combining experimental data with modelling and advanced data processing and analytics methods will accelerate that understanding.

## 1. Introduction and background

Additive manufacturing presents a potential opportunity to introduce a paradigm shift in component design. The ability to locally tailor processing paths allows for new sophisticated designs that incorporate complex geometries with heterogeneous processing, leading to spatially varying material properties. Properly accounting for, and ultimately exploiting, this processing heterogeneity requires the ability to link the local processing state to properties and performance of the local material. Current geometry-based design approaches, such as topology optimization, do not directly account for material property evolution as the geometry is built. Most commercial additive manufacturing systems utilize fixed scanning strategies that are highly sensitive to the build geometries, resulting in potentially unavoidable changes in the local processing state. Understanding and accounting for the interaction of the component geometry with the predetermined machine scan path is critical to predicting material structure, and thus material properties. This understanding is necessary to ensure tools such as topology optimization properly account for heterogeneous material properties. An understanding of the interactions between component geometry, the processing path, and material structure is an enabling factor in the development of scan path optimization for tailored, spatially varying materials properties.

The complexity of machine scan paths and the control provided to the manufacturing engineer varies among the different printing systems. In general, most commercial machines divide the build plate into subdomains and then process them in some global order. Figure 1 shows an example of the scanning strategy employed by an EOS M280 laser powder-bed fusion machine. Two consecutive layers are colored by the time at which the laser was at each given point in space. The solid bands of apparent common color highlight a macroscopic serpentine pattern that divides the build plate into lanes termed



‘stripes’. The user has the ability to change the width of these stripes at build time. Within the stripes, a finer-scale serpentine pattern exists in which the laser moves perpendicular to the long axis of the stripe. When the beam reaches one side of the stripe, it may, under certain user conditions, shut off, turn around, turn back on again, and then scan to the other side of the stripe. These individual scan vectors within a given stripe are termed ‘hatches’. Similar to stripes, the user may change the spacing between neighboring hatches at build time. The global scan path is predetermined by the machine and covers the entire build plate; the only influence of the intended build geometry occurs when the hatch vectors intersect the triangulated surface mesh that defines the build, which determine when the laser is on. Figure 1 clearly shows artificial interfaces inserted within the build geometry between neighboring stripes, termed ‘stripe boundaries’. The machine offers parameters to control the overlap of neighboring stripes, affecting the structure of these interfaces. The global scan path is rotated for each successive layer by a user-prescribed angle to ‘randomize’ the volumetric scan path and prevent alignment of the stripe boundaries throughout the build. A key observation from figure 1 is that the local processing path of any given point in each part is a convolution of the global scan path, the part geometry, and the geometry and relative placement of other parts in the bed.

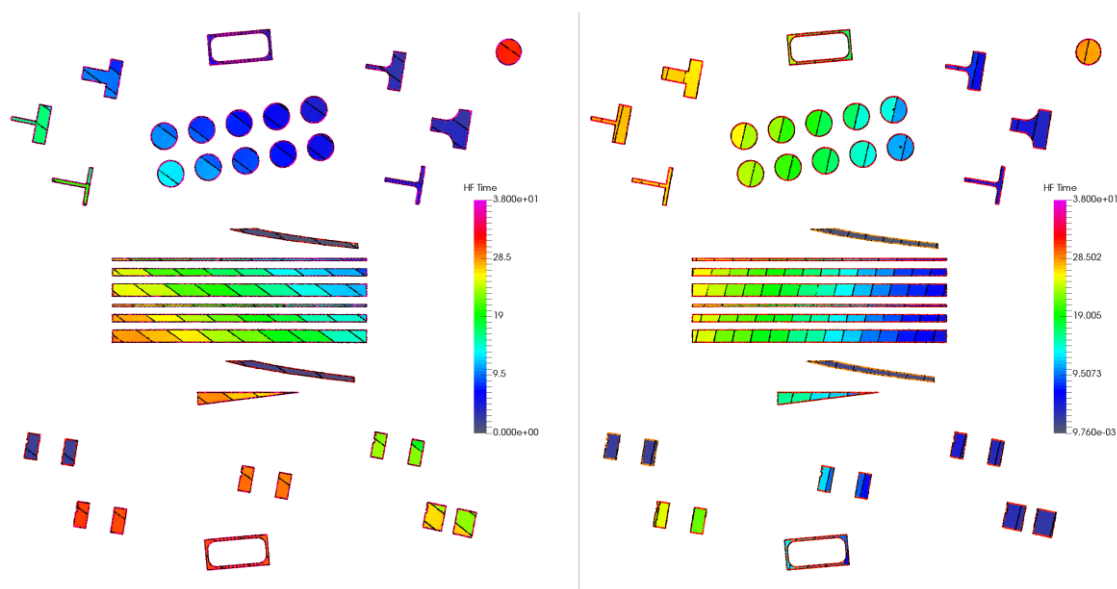


**Figure 1.** Two consecutive layers in a laser powder-bed fusion build displaying the time at which the laser was present at each given point in space. The macroscopic serpentine pattern of the laser raster is seen and the rotation between consecutive layers is apparent. The influence of scan path and part layout on local processing path is evident in the part at the lower right of the build plate, where it is entirely printed within a single second on one layer and takes approximately five seconds on the other layer.

In this paper, we discuss multiple characterization methods applied to samples produced by two different metallic additive manufacturing processes, namely laser powder-bed fusion (LPBF) and electron beam melting (EBM). Given the complexity of scan paths, particularly the variability between systems and the interaction of component geometries, we develop a methodology that couples experimental data and modelling to convert the scan paths into spatially resolved local thermal histories. Finally, we present initial findings on the correlations between local processing history microstructure, and defects in the two different printing processes.

## 2. Materials, Processes and Features of Interest

In this work, we have selected two sets of samples from two different processing techniques, LPBF and EBM. Each set of samples originates from a single build in the given process. A titanium alloy, Ti-6Al-4V, was used in both processes. Figure 1 shows the layout of specimens in the LPBF build. The

samples are mostly 2.5-dimensional, extended in the build direction, which is normal to the plane of figure 1. Two components from the LPBF build are showcased in this paper: the cylindrical object in the upper right corner of the build layout, and an arch, shown as two rectangles in cross-section at the lower right corner of the build layout. The LPBF samples were investigated in an attempt to correlate the presence of voids to the local processing conditions.

Figure 2 shows the layout of the EBM build, with arrows denoting the samples showcased in this work. These two samples were taken from groups of plates arranged in an attempt to force a modulation in local processing condition. The EBM process was performed on an ARCAM A2, in which the power and speed of the beam is determined based on line length to be melted on any given scan vector. The bulk scan vectors always point in the positive or negative  $x$  or  $y$  directions and span the run from one edge of the build plate to the other. The layout of the build shown in figure 2 suggests that the group of larger plates will have a longer melted line length on every layer regardless of the scan vector directions, thus experience processing with consistently higher power and speed compared to the smaller plates. The microstructural feature of interest in these samples is the macroscopic texture and its dependence on local processing history.

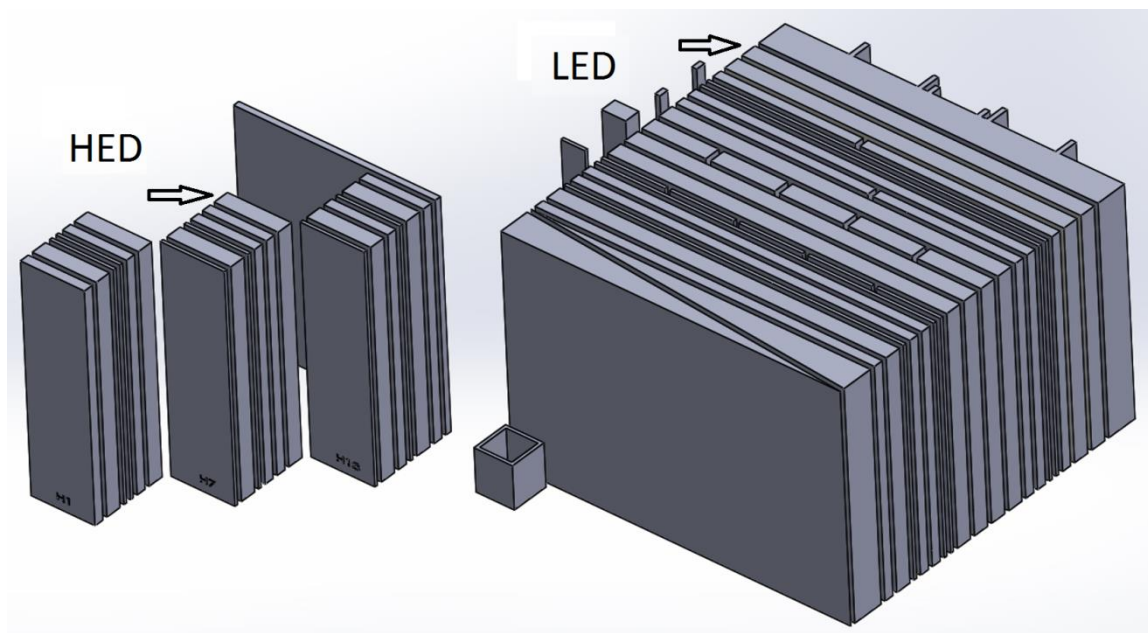


**Figure 2.** Layout of Ti-6Al-4V EBM build with investigated samples noted by arrows. High energy density (HED) and low energy density (LED) regions described in Section 6.2 are indicated.

### 3. Characterization techniques and data streams for analysis of additive manufacturing

A distinct advantage of additive manufacturing over many traditional manufacturing processes (i.e., forging or casting) is the abundant amount of data available from the process. In this work, we have data characterizing the prebuild intent, in-situ processing, and post-build structure. This section introduces the data streams available and explains why they were included in this analysis.

#### 3.1. Build geometry

The intended build geometry is represented as a triangulated surface mesh of the part(s) to be built, typically in the form of a Stereolithography file (.stl). The surface mesh is ‘sliced’ by the software that controls the additive manufacturing system at the build layer thickness, resulting in 2D polygons on each print layer; the beam will be on inside of the polygons and off outside of them. The surface mesh is a discrete representation of a possibly smooth design, presenting a potential trade-off between fidelity to the original design, the size of the mesh, and the resolution that the printing system can practically

achieve. It is important to note that the build geometry represents the intended geometry of the part(s); the actual printed part(s) may not correspond exactly to this geometry due to numerous factors, including residual stresses and distortions, build errors, and machine calibration errors. In this work, the intended build geometry is available for both builds.

### 3.2. *Process intent and monitoring*

During the printing process, the beam is rastered across the build plate in a potentially proprietary manner. If the machine does not supply the scan path of the beam directly, prior knowledge of the scan strategy or a third-party monitoring system is required to obtain the full path history. In addition to tracking the path of the beam, some monitoring systems also utilize additional sensors attached to the system to monitor temperature, oxygen levels, sound, beam power and voltage, and emitted light from the molten pool. In this work, the scan path is obtained via different routes for the two printing systems. In the EBM process carried out on an ARCAM A2, the scan path with voltage and speed levels was determined by internal knowledge of the scan strategy through collaboration with Oak Ridge National Laboratory's Manufacturing Demonstration Facility (ORNL MDF) and the system manufacturer. The scan path is represented as a set of scan vectors with known power and speed. In the LPBF process, a third-party monitoring system (PrintRite3D from SigmaLabs) was used to track the position of the beam, along with its power and drive, sampled at 50 kHz. In addition to tracking the beam and its properties, the PrintRite3D system measures the amount of emitted light through a photodiode on axis of the laser, the temperature of the chamber, the oxygen level of the chamber, and an audio signal within the chamber. The PrintRite3D data is represented as a point cloud of locations of the beam at discrete points in time. These data streams from the two processes were used to track the local processing history within the build chamber.

### 3.3. *Computed tomography (CT)*

After printing, it is often desired to inspect both for dimensional accuracy and for defects (i.e., voids or lack-of-fusion). Computed tomography (CT) is a common tool for non-destructively inspecting metallic components. CT is capable of quantifying measureable density gradients within parts, but has some limitations with respect to spatial resolution. It can be difficult to investigate large volumes of material with high spatial resolution using laboratory-scale CT, since the volume of inspected material is coupled inversely to the spatial resolution. Due to this limitation, surface roughness is difficult to quantify using CT, and small defects ( $< 50\mu\text{m}$ ) are often not detected in samples larger than a few cubic centimeters. Furthermore, the complex geometries that can be printed with additive manufacturing present significant difficulties for CT reconstruction. The most common techniques for CT reconstruction, such as filtered back projection, often exhibit noticeable artifacts when applied to complex or highly anisotropic parts[1]. For this work, the relatively small LPBF samples were inspected using CT: the simple geometric form of the samples and the overall small volume allows for a reasonable spatial resolution ( $\sim 23\mu\text{m}$ ) for inspecting the defects of interest.

### 3.4. *Mechanical serial-sectioning with optical microscopy*

Volumetric inspection via serial-sectioning decouples spatial resolution from the volume of inspected material, offering a distinct resolution advantage over CT while also being free from reconstruction artifacts. However, the technique is destructive and time intensive. For the investigation in this work, the imaging mode employed on each exposed section was optical microscopy (OM). OM is well suited for clearly differentiating voids in metallic samples. The LPBF sample was serial-sectioned for a relatively small volume to compare with CT. The sample inspected with serial-sectioning was imaged at approximately 10x the resolution of CT, using  $1\mu\text{m}$  section thickness with  $2\mu\text{m}$  in-plane OM pixel size. Single 2D optical images were collected for the EBM samples, but no serial-sectioning was performed on those samples.

### 3.5. *Electron backscatter diffraction (EBSD)*

EBSD is a scanning electron microscope (SEM) technique that is capable of deducing the crystallographic orientation of locations within a sample [2]. If performed at sufficient spatial resolution, individual grains can be resolved and their morphologies characterized. If EBSD is performed with a coarser spatial resolution, individual grains may be difficult to characterize, but the meso-to-macroscopic texture of the sample can be obtained. In this work, the EBM samples were inspected with EBSD. The resolution of the inspection was selected to allow for large area coverage in an effort to quantify macroscopic texture, but within reasonable time constraints. Some selected areas were inspected using a finer resolution to determine the general morphological characteristics of the grains. The prior beta grains, whose orientation distribution was the focus of this work, were relatively large and well-sampled by the chosen resolution.

#### 4. Registration and fusion of data streams

The various data streams must be registered, or brought into spatial coincidence, to assess correlations between process and structure at specific locations. Registration of the data streams is complicated by two factors. First, the data element dimensionality varies from 0D (point clouds) to 2D (surface meshes) to 3D (image grids). Second, the data streams contain different information content that does not necessarily correlate. Thus, utilizing correlated information approaches, such as mutual information, to register the data sets could bias subsequent analyses. Ideally, the samples would contain some independent reference marks detectable in each of the data sets, which could aid registration without introducing bias. For this work, these 'reference marks' were selected to be the sample surfaces themselves. Since each data stream provides an inspection of the part geometry at a different processing step, the sample surfaces are not guaranteed to all match exactly. The surface mesh is the intended part geometry, the in situ monitoring data is where the beam rastered (which may have offsets to account for distortions and melt pool size estimates), and the CT data captures a measurement of the physical build (which could be affected by residual stresses and distortions, artifacts in the CT reconstruction, and from cutting the sample off from the build plate). Therefore, an iterative registration procedure was used to find the transformation that best brings the data streams into spatial coincidence.

The first step in the registration process is to identify 'key points' in each dataset that correspond spatially; this step involves extracting out points that represent the part surface. The second step is to use some algorithm to determine the translations, rotations and distortions necessary to bring the key points into coincidence. In the LPBF work, the iterative closest point (ICP) algorithm, implemented in the open source Point Cloud Library (PCL), was chosen to determine the necessary transformation [3,4]. The iterative closest point algorithm takes as its input the set of key points that represent the part surface. The build geometry surface mesh directly defines the sample surfaces, so each triangle was point sampled uniformly within its area. To generate an unbiased surface sampling, triangles to sample are selected randomly from the surface mesh weighted by their area. The CT data sets were thresholded using a local gradient approach to determine the voxel faces that were at the surface of the sample [5]. Those voxel faces were then triangulated and smoothed using a Laplacian surface smoothing algorithm [6] to yield a surface mesh of the printed sample. This surface mesh was then sampled in the same manner as the build geometry surface mesh. Finally, the point cloud from the PrintRite3D monitoring system was uniformly dense throughout the sample, but only the sample surface was desired for the registration. In order to identify the sample surface, a Delaunay tetrahedralization was performed using PCL and the concave hull defined by the surface triangles of the tetrahedralization was identified [7]. The points that defined the concave hull were retained as the surface of the sample. Figure 3 shows the extracted surface points and the resultant registration for an arch-shaped object from the LPBF build (lower right corner of figure 1). In the EBM work, the process intent data were directly obtained from the build geometry, and thus already shared a common reference frame. The texture information extracted from the EBSD scans of the EBM builds was associated with each sample at the macroscale, so no registration was performed to correlate with local scan path. Rather, the processing of the two samples was generalized by investigating a single point in the center of each sample. The scan strategy of the EBM process combined with the build layout makes this approach reasonable for the present analysis.

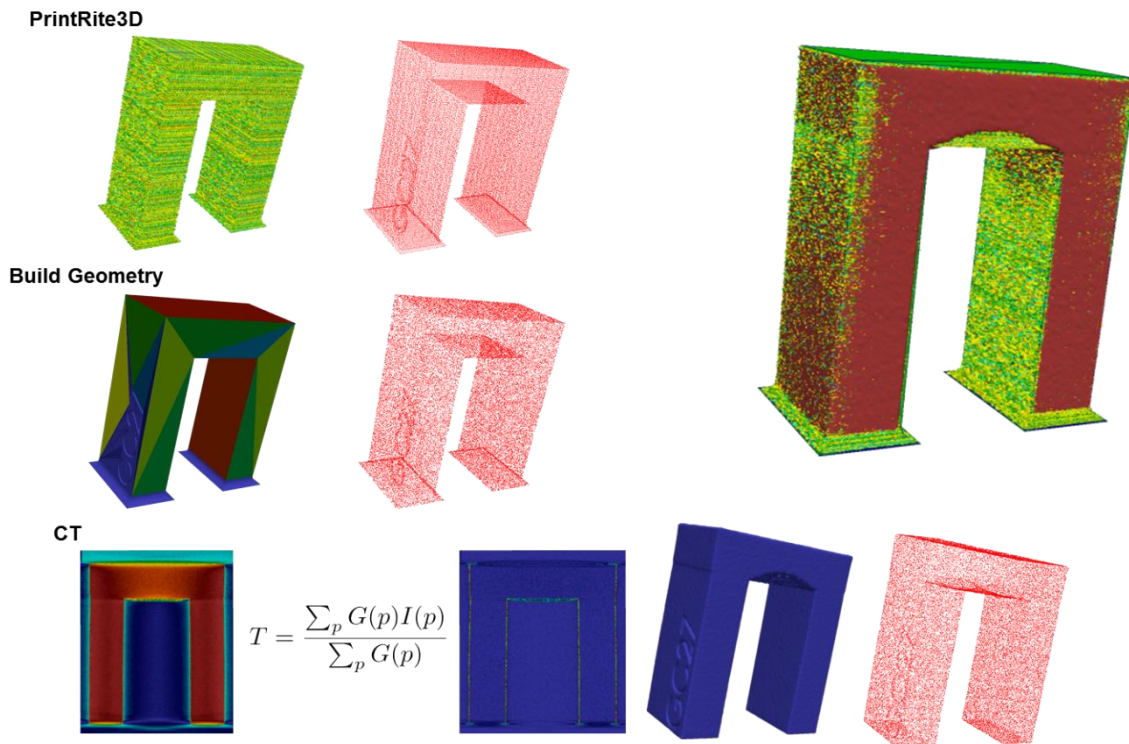


**Figure 3.** Data streams from CAD, CT and PrintRite3D, with point representation of sample surface. Larger inset shows final registry of full PrintRite3D data (green and yellow points) overlaid with threshold CT data (maroon surface) and CAD surface mesh (green triangles with blue edges on top surface). Note the point representations of the sample surface in the individual datasets are in their own reference frame and do not illustrate the magnitude of initial disregistry.

### 5. Modeling material thermal histories from complex moving heat sources

Local thermal history is an important quantity to consider during development of additive manufacturing processes for metallic materials as it affects microstructure, residual stresses, and defects. Depending upon the specific problem, the range of physical phenomena and energy transport mechanisms involved can be extensive: conduction, buoyancy and surface-tension-driven fluid flow, the associated convective thermal transport, beam-material interactions, radiative thermal transport, and phase changes including evaporation. While they can generate considerable insight, high-fidelity solutions to such multi-physics computational problems are often expensive to compute, and thus fast-acting physics-based models have been developed that make simplifying assumptions. An example of such an analytical model is the so-called Rosenthal's solution [8]. This analytic solution describes the temperature field induced by a point source moving uniformly across a semi-infinite body, allowing only thermal conduction as the transport mechanism, and assuming temperature-independent thermo-physical parameters. This model is computationally inexpensive and the solutions exhibit many qualitative features that are also seen empirically. However, the Rosenthal resolution presents several issues. First, the energy input is a point source, so the energy input flux is effectively infinite at that point location, which then induces a temperature discontinuity. Secondly, the energy source moves uniformly in space, so the model effectively describes steady-state deposition of a single pass, and cannot describe transient effects such as beam direction changes, or modulations of power or speed. The substrate is semi-infinite, which is not unreasonable for short times, but may be unreasonable for long times compared to the thermal diffusion time scale. Finally, the assumption that thermal conduction is the only transport mechanism is flawed. Again, despite these limitations, this

model is qualitatively useful and predicts many trends that are observed empirically (e.g. melt pool width scales like power over velocity, aspect ratio scales with power times velocity, etc.).

A number of other researchers expanded the model of Rosenthal by replacing the point source with a distributed energy source [10-14]. This effectively regularizes the temperature discontinuity in the Rosenthal solution immediately under the energy source. The solutions given by the two approaches converge for locations sufficiently far from the source (typically several beam diameters). While these expanded solutions admit a field maximum temperature that circumvents the temperature discontinuity, the remaining issues are still present. Furthermore, while the temperature does remain finite, the peak value is often unrealistically high when practical deposition parameters are considered, on the order of 10,000 K or higher.

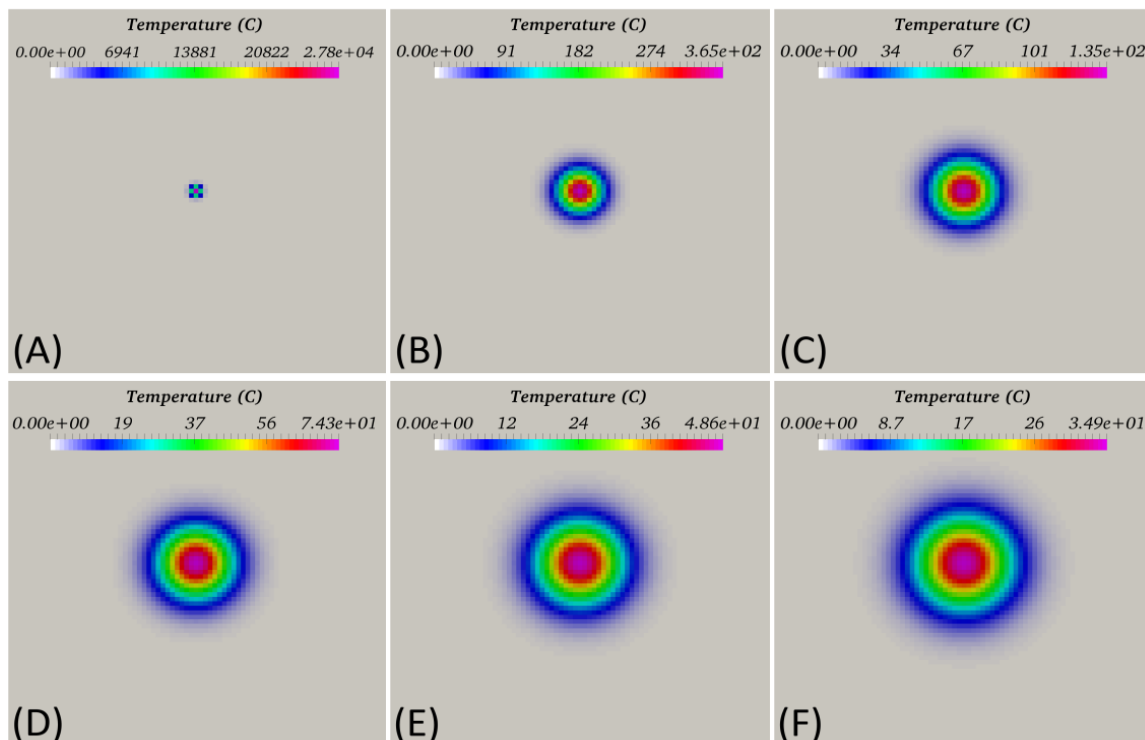


**Figure 4.** Sequence of time steps from the solution of a single discrete point source (A) 0.00002s, (B) 0.0002s, (C) 0.0004s, (D) 0.0006s, (E) 0.0008s, (F) 0.001s. Note the change in the temperature scale between time steps. (A) Illustrates the unrealistically high temperatures observed instantaneously after the source becomes active. Each panel has a 1mm x 1mm field-of-view.

The main goal of this work is to develop a computationally inexpensive thermal model that relaxes constraints on beam path and allows for transient conditions, including arbitrary beam motion and modulation of deposition parameters. Secondly, we wish to estimate and include these in a 'global' sense. The first major simplifying step is to represent the continuously moving source as a series of discrete stationary energy pulses. The pulses are positioned spatially by sampling the location of the continuously moving beam at a fixed rate, placing sources at these locations, and activating them at the time the beam passes. This approach implicitly captures velocity and sequencing, while reducing the complexity of the modeling approach. We choose individual source terms to be Gaussian in space, centered at locations  $\vec{r} = (x_i, y_i, z_i)$  which the beam visits at times  $\tau_i$ :

$$s_i(\vec{r}, t) = \frac{A_i \delta(t - \tau_i)}{(2\pi\sigma^2)^{3/2}} \exp\left(-\frac{(\vec{r} - \vec{r}_i)^2}{2\sigma^2}\right)$$

Here  $A_i\delta(t-\tau_i)$  is the power of the source with the Dirac delta function having units of inverse time,  $\sigma$  controls the physical size over which the energy is deposited, and  $r_i$  and  $\tau_i$  are the position and time of the  $i^{\text{th}}$  discrete source. All the energy of the  $i^{\text{th}}$  discrete source is deposited at time  $t = \tau_i$  and then made inactive, though its deposited energy continues to influence the system for all times  $t > \tau_i$ . If we integrate each point source over the full time and space we get:

$$\int_t \int_{\bar{V}} s_i(\vec{r}, t) dt d\vec{r} = \int_{\tau_i}^{\tau_i+\Delta t} P_i dt = P_i \Delta t$$

where we consider the half space  $\bar{V}$  that includes only points where  $z \leq 0$  if the source is at  $z = 0$  and  $\Delta t$  is the time elapsed between activation of sources. Substituting into the transport equation gives:

$$\frac{\partial T}{\partial t} - \alpha \nabla^2 T = f(\vec{r}, t) = \sum_i^N \frac{2P_i \Delta t}{\rho c_p} \frac{1}{(2\pi\sigma^2)^{\frac{3}{2}}} \exp\left[-\frac{(\vec{r} - \vec{r}_i)^2}{2\sigma^2}\right] \delta(t - \tau_i)$$

Note the factor of two that comes from the fact that half of the energy contributed by the source is deposited above the  $z = 0$  plane and the energy must be effectively doubled to ensure the energy distributed below the plane of symmetry is equivalent to the true continuous source.

To solve the transport equation, we use a Green's function approach with linear operator:

$$\mathcal{G}(\vec{r}, t | \vec{q}, s) = (4\pi\alpha(t-s))^{-3/2} \exp\left[\frac{-(\vec{r} - \vec{q})^2}{4\alpha(t-s)}\right]$$

and the solution is given by:

$$T(\vec{r}, t) = \int_V \int_t \mathcal{G}(\vec{r}, t | \vec{q}, s) f(\vec{q}, s) d\vec{q} ds$$

Finally, executing the integrals, the temperature is given by:

$$T(\vec{r}, t) = \sum_i^N \frac{P_i \Delta t \Theta(t - \tau_i)}{\rho c_p \sqrt{2} [\pi(\sigma^2 + 2\alpha(t - \tau_i))]^{3/2}} \exp\left[-\frac{(\vec{r} - \vec{r}_i)^2}{2\sigma^2 + 4\alpha(t - \tau_i)}\right]$$

where  $\Theta$  is the standard Heavyside step function. Figure 4 shows the solution of a single discrete point source while figure 5 shows the solution of a series of discrete point sources approximating a moving source.

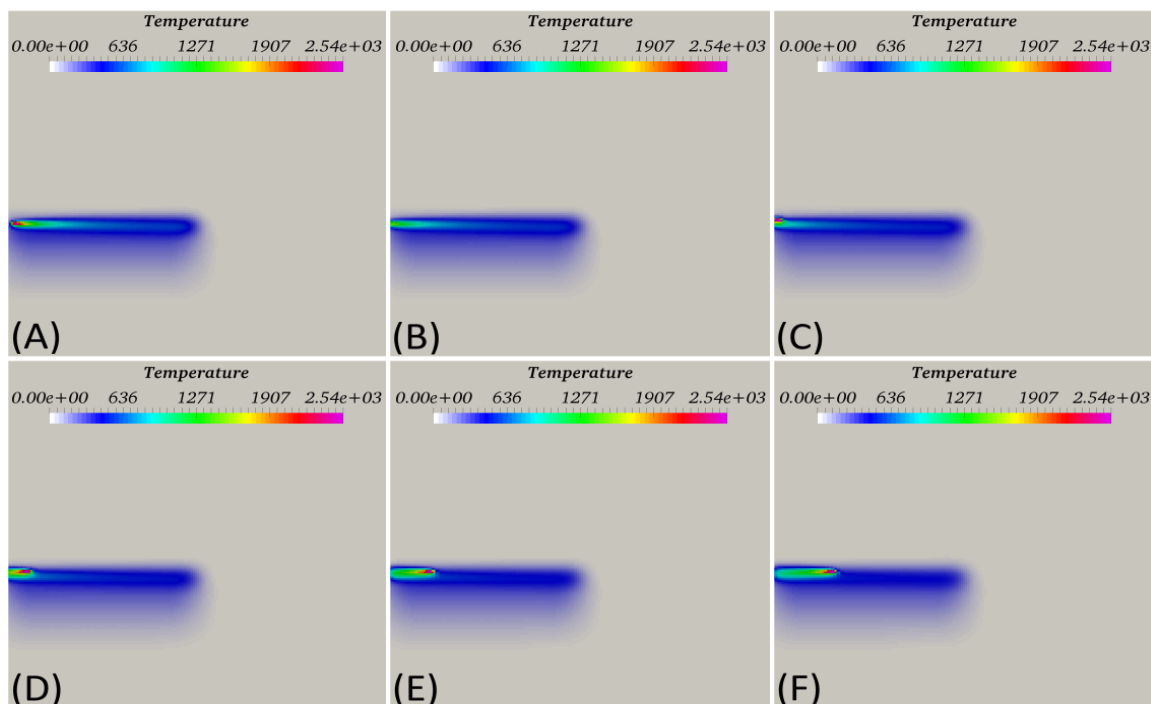


**Figure 5.** Sequence of time steps from the solution of a set of discrete sources turning on sequentially to represent a moving source. In the sequence, the beam approaches the edge of the region to melt (A), shuts off (B), turns around and turns back on (C), then moves away from the edge towards the other side of the region (D)-(F). The field-of-view of each panel is 14mm x 14mm. The model captures the shape of the melt pool and its dynamic size as the beam moves in a representative scan path. Note the disappearance of the melt pool immediately after the beam shuts off in (B).

## 6. Results and analytics

### 6.1. Voids in LPBF of Ti-64

CT investigation of the 10 mm cylindrical sample printed by LPBF (upper right corner of figure 1) is shown in figure 6a. The CT scan shows a significant amount of porosity that appears irregularly dispersed when looking at the entire sample. However, when a subsection of the sample is viewed (figure 6b), it is clear that the voids are correlated and often form linear arrays. The locations of the internal stripe boundaries are added in figure 6c, by displaying the points where the beam is turning around. It is clear that the linear arrays of voids coincide with these stripe boundaries.

The resolution of the CT reconstruction shown in figure 6 was 23  $\mu\text{m}$ , so voids smaller than  $\sim 50 \mu\text{m}$  are generally undetected and voids smaller than  $\sim 200 \mu\text{m}$  do not have their shape well represented. The voids appear nearly equiaxed, unlike ‘lack-of-fusion’ voids that tend to be planar in nature. Higher resolution imaging was needed to inspect the nature of the voids. Serial sectioning using a 1  $\mu\text{m}$  slice spacing was performed for a sub-region very close to that shown in figure 6b. Optical microscopy montage images were taken on each exposed section, using an in-plane resolution of 2  $\mu\text{m}$ . A single optical image montage is shown in figure 7a, and the same region from the CT image is shown in figure 7b. The higher resolution image montage shows the same linear arrays as the CT image, as well as a secondary population of smaller, elongated voids. The void shapes are more clearly discernible in figures 7c and 7d. The second, smaller void population, which was generally below the detectability of the CT reconstructions, is aligned perpendicular to the arrays of larger voids. These smaller voids correspond with the individual hatches oriented perpendicular to the stripe boundaries. The morphology of the second population is indicative of lack-of-fusion porosity resulting from insufficient melt pool size, which prevents the fusion of neighboring scan melt pools. Figure 7 also shows a denuded zone of

relatively dense material separating the smaller lack-of-fusion voids from both the external surface of the cylinder and the larger stripe boundary defects. Finally, in figure 7c, the larger voids appear to have a characteristic “D” shape, where the left side of the void is flatter than the right side. This characteristic is seen on many of the linear arrays.

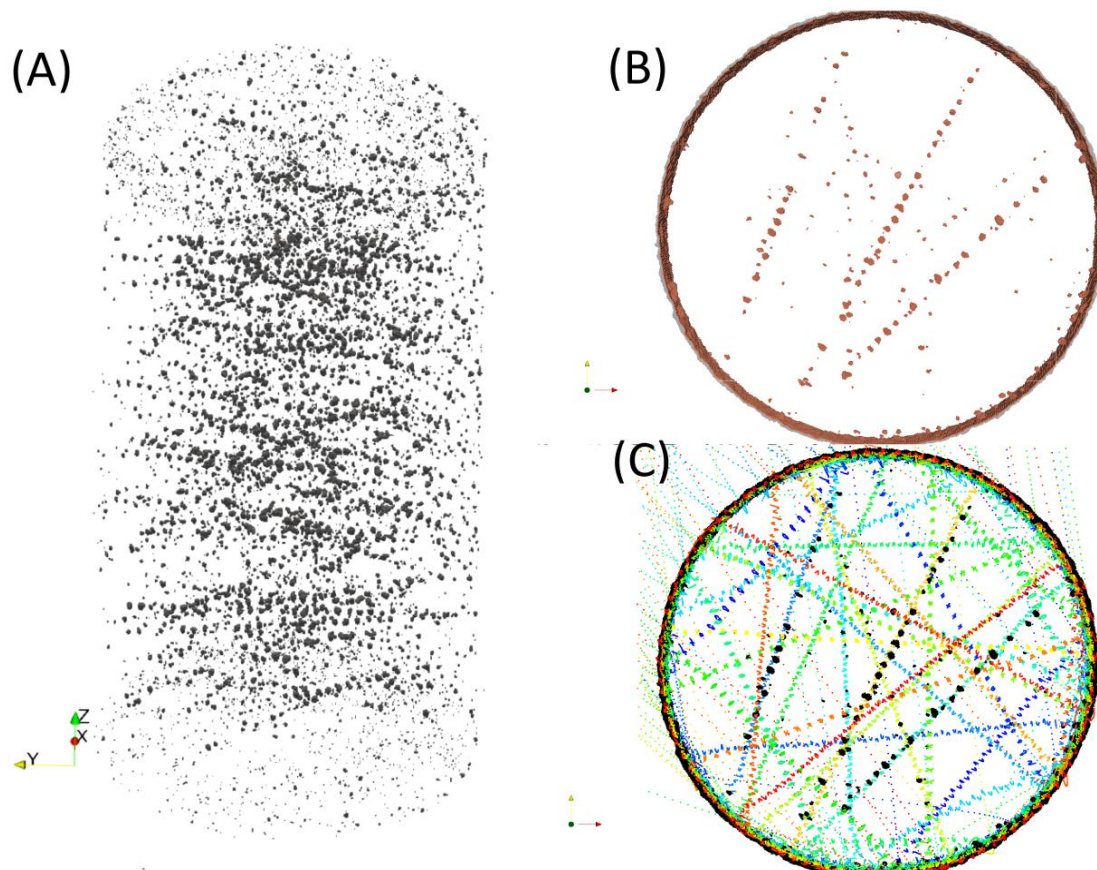


**Figure 6.** (A) Threshold reconstruction of CT scan of 10mm diameter, 20 mm tall cylindrical sample showing the internal porosity in the sample, (B) 1mm thick sub-region taken from the central portion of the cylinder showing the voids arranged in linear arrays, and (C) Overlay of the voids from (B) and the internal ‘stripe boundaries’ on the printed layers in that sub-region. Note the linear arrays lay on boundaries, but not all boundaries align with arrays of voids.

To understand the “D” shaped voids in figure 7c, the raw monitoring data were overlaid with the optical montage. Examination of the combined data revealed that the material viewed at the left side of image was printed after the material view on the right side. Further, the voids line up with the end of scan vectors associated with printing the left side material. Because this image is from a section through the bulk of the cylinder, additional material would have been built on top of the defects. The top surface of the part can be investigated to observe a material layer that experienced only one laser pass. Figure 8a shows an image of the top surface of a part from this build. The image clearly shows a repeating pattern of “D” shaped features. Figures 8b-d show a single scan vector from above and sections through the track at the middle and end, showing that the divot is present at the end of the track.

End of track defects have been seen in higher-fidelity models that account for evaporation, convection, and fluid flow within the melt pool [15]. Using our model, we are able to determine the amount of time any point in space spends within the melt pool. Figure 9 shows discrete points along a series of scan vectors, colored by the amount of time that the material was molten at each position.

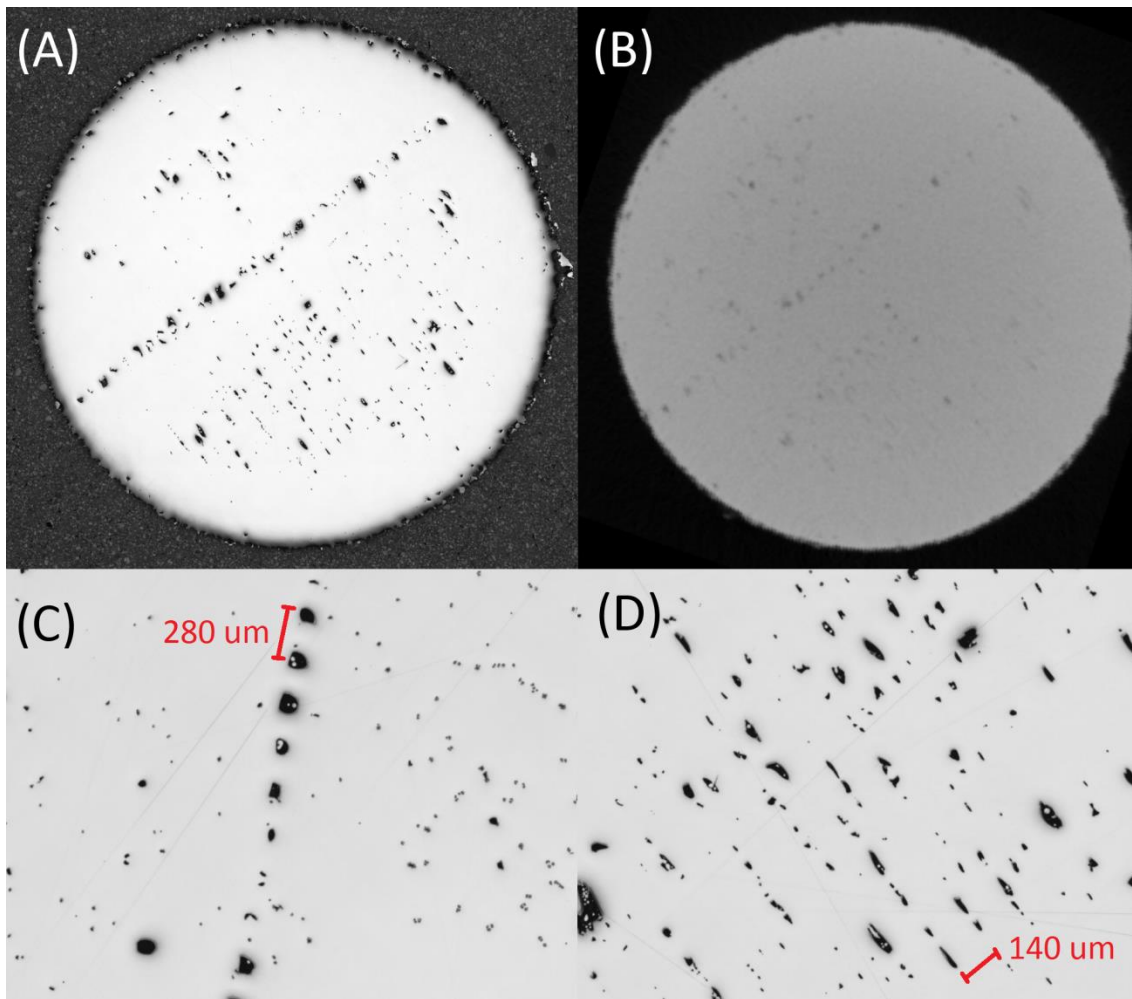


**Figure 7.** (A) High resolution optical microscopy montage showing the morphology of two populations of voids – montage covers the entire 10mm diameter of the part, (B) Section from CT reconstruction at same position as montage in (A), (C) Sub-image showing morphology of linear void arrays, and (D) Sub-image showing morphology of smaller, more elongated void population.

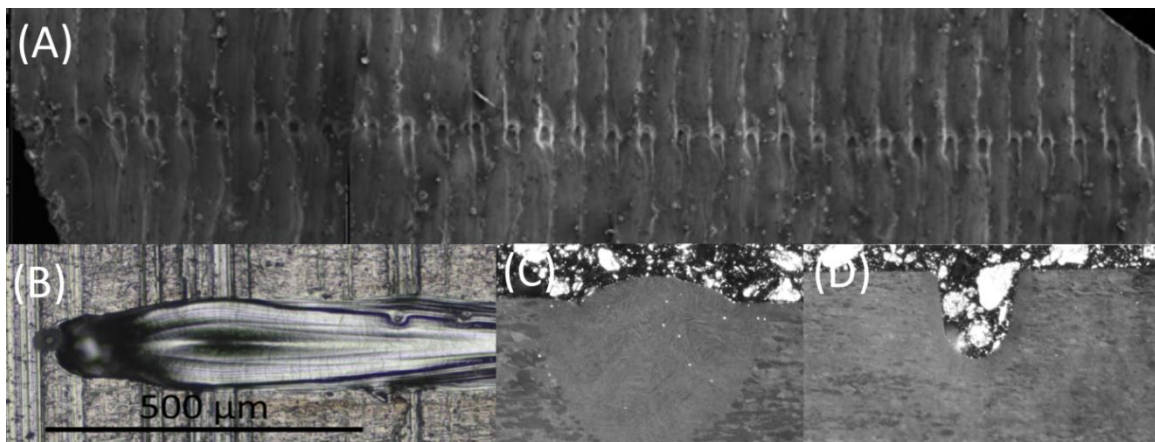


**Figure 8.** Images showing end-of-vector defects. (A) Top surface of sample from LPBF build, (B) Top view of single laser scan pass, (C) perpendicular section through track in (B) at midpoint along track, and (D) perpendicular section through track in (B) at endpoint where divot is present.

Points along the scan vector spend progressively less time being molten as the laser approaches the turning position. At stripe boundaries, or at the perimeter of the part, where the beam also turns off and back around, there is a periodic pattern that mirrors the pattern seen in figure 8a. As explained in [15], the molten pool solidifies too quickly and is not able to fill in the divot at the end of the track, leaving a defect. The time to solidify is material specific, depending on its thermal properties and freezing range, but for the present alloy at the power and speed values used during printing, the model appears to predict times in reasonable agreement with freezing in an end-of-track defect.

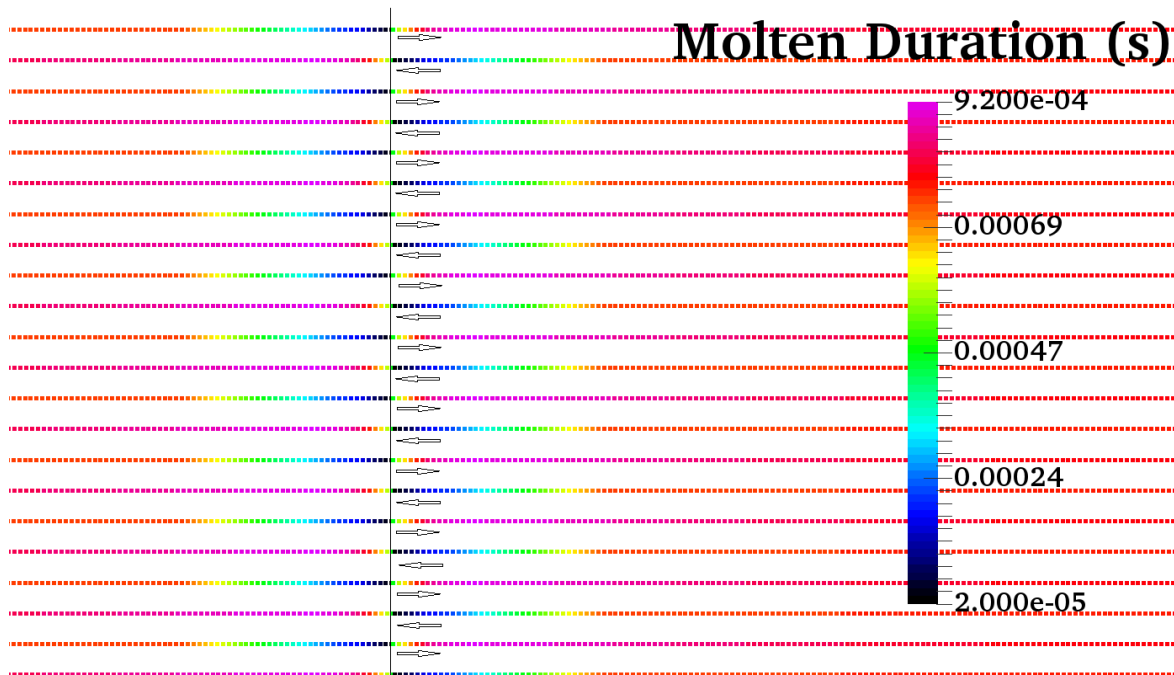


**Figure 9.** Discrete points along a set of scan vectors showing the time each point spent in the moving molten pool. The thin black line shows the position of the stripe boundary and the arrows show the direction of the beam into and out of the turn-around at the stripe boundary. The time spent molten decreases as the beam approaches the end of the track, leading to the ‘freezing in’ of a defect.

The smaller voids along the hatch vectors that appear to be lack of fusion defects were also correlated to phenomena seen in the thermal model. Figure 10 shows points along scan vectors, similar to figure 9, but with the points colored by the temperature of the point just prior to the laser passing through it (i.e., the pre-heat level prior to melting). The offset in time was selected to be the time it takes the beam to move two melt pool diameters, or about 1/5000 seconds. The figure shows that the preheat temperature is highest coming out of a turn-around, but inset from the stripe boundary or perimeter of the part. This offset results from the beam traveling faster around the turn than the heat diffusion from the previous hatch vector. The preheat temperature is directly related to the maximum width that the melt pool will achieve at that point, albeit not in a linear fashion. As a result, the individual scans do not produce a uniform width track, but rather one that narrows as the track progresses. The middle of the stripe is where the two neighboring tracks would both have narrowed and potentially created the possibility of a lack of fusion void, if the energy density were not sufficient. Figure 10 shows a region in the middle of the stripe that exhibits significantly lower preheat compared to the areas near turn-arounds, resulting in smaller melt pool widths that mirror the voids shown in figure 7d.

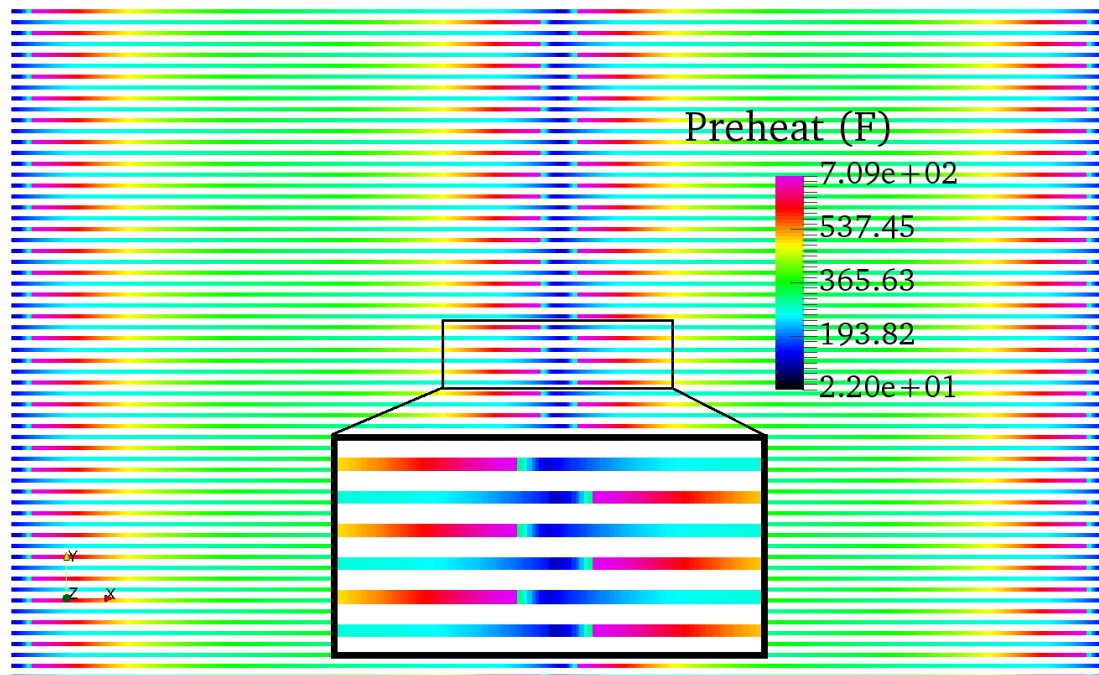


**Figure 10.** Discrete points along a set of scan vectors showing the temperature just prior to the laser passing through the point. The edges of the image are the perimeter of a square object and the region in the exact middle of the object is a vertical stripe boundary. The ‘preheat’ temperature is at a maximum for any given scan vector just after (approximately 1-2 mm) it turns on following completing a turn-around at a stripe boundary or the outer boundary of the part. The middle of the stripe is uniformly preheated relative to the regions near turn-arounds, which have both high and low preheats.

### 6.2. Microstructure and texture of EBM Ti-64

The layout of the EBM build investigated in this work was designed to push the processing conditions into two extremes. The group of smaller plates at the left of the layout in figure 2 were processed with a lower power and velocity, but a higher energy density than the larger plates at the right of the layout. For this section, the two samples will be referred to as the high energy density (HED) and low energy density (LED) samples. EBSD scans of the HED and LED samples are shown in figure 11 along with the computed pole figures. There is a noticeable change in texture between the two samples, with the HED sample exhibiting a typical texture [16] and the LED sample showing an ‘abnormal’ texture for the EBM process.

The scan vectors for the EBM build were input into our thermal model: the result of a representative layer is shown in figure 12. The layout of the build was such that the melt pool size and shape were relatively consistent on all layers, so for simplicity of viewing, we show a single 2D layer; note that the thermal solution is fully 3D. In the figure, a spatially-resolved temperature map is shown for a snapshot in time for the two samples. Additionally, a time-temperature plot is shown for a single point near the middle of the two samples. The spatial maps show that the melt pool and thermal field have a much higher aspect ratio in the LED sample. The time-temperature plot shows that the time above the melting temperature and cooling rate through the beta transus is longer for the HED sample. Additionally, the gradients in the thermal fields, normal of the melt pool interface, and velocity of the melt pool interface differ in the two samples. The curvature of the melt pool is larger in the LED sample, with smaller re-melt depth. The velocity of the melt pools, which affects the dominant grain growth direction, differs between the two samples. For both samples, the grains appear to grow in a columnar fashion with the long axis parallel to the build direction. However, upon higher resolution investigation of the grains in the LED sample, it is seen that the grains grow in a serrated manner, exhibiting periodic patterns associated with multiples of the layer thickness and the scan rotation strategy of the system. Figure 13

shows an EBSD map and a reconstruction of the prior beta grains from the alpha orientations [17]. The EBSD scan is perpendicular to the build direction and the grains have been annotated to show the dominant growth direction deviating from the build direction by approximately 30°.

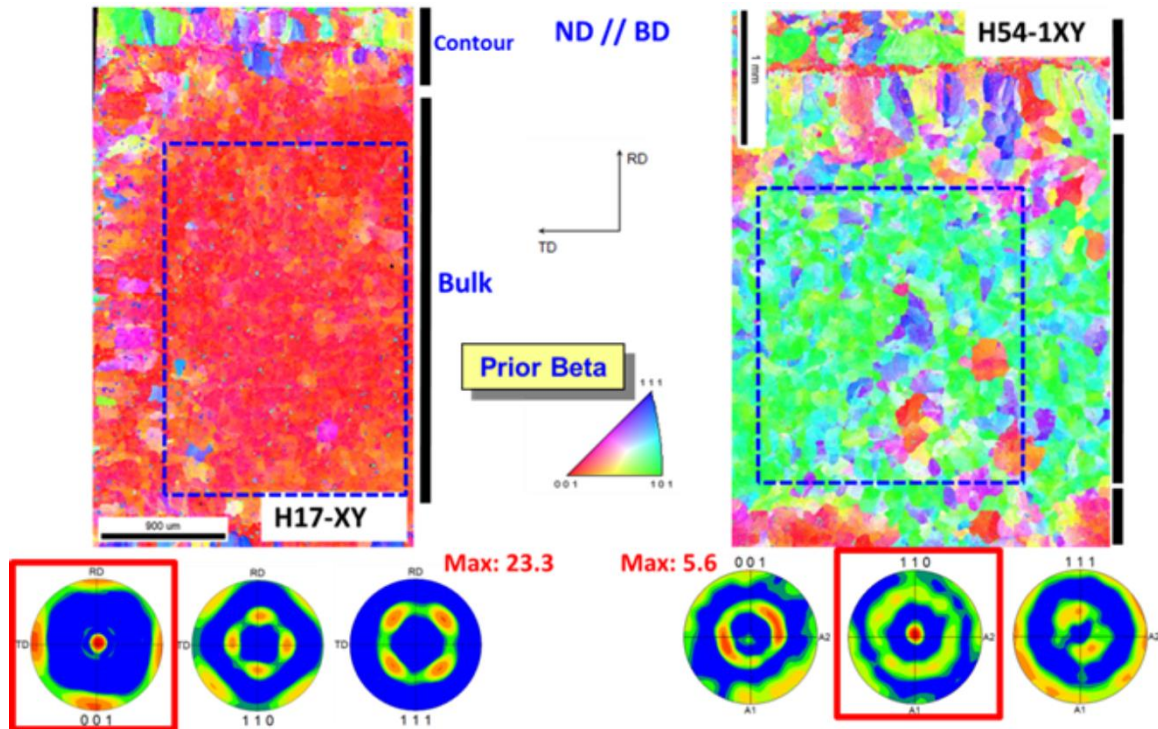


**Figure 11.** EBSD scans and pole figures for the HED (left) and LED (right) samples from the EBM build. The texture of the HED sample is ‘typical’ for EBM Ti-64, while the LED texture is ‘abnormal’. Note the build direction is normal to the plane of the scan.

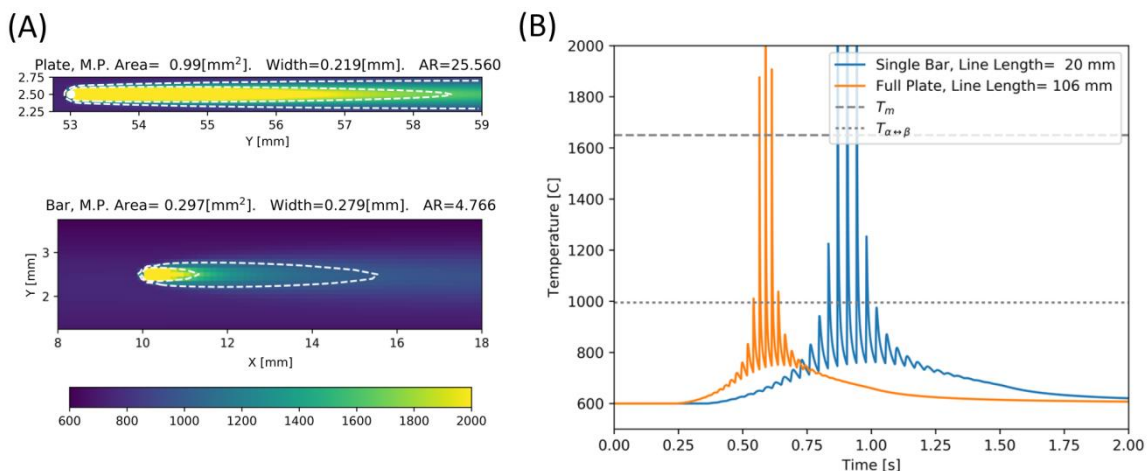


**Figure 12.** (A) Spatially-resolved thermal fields for a representative layer in the EBM build for the HED (bottom) and LED (top) regions, as calculated by the thermal model and (B) Time-temperature plots for a single point in the HED (blue) and LED (orange) regions. Note the differences in time above the melting temperature and the cooling rate across the beta transus.

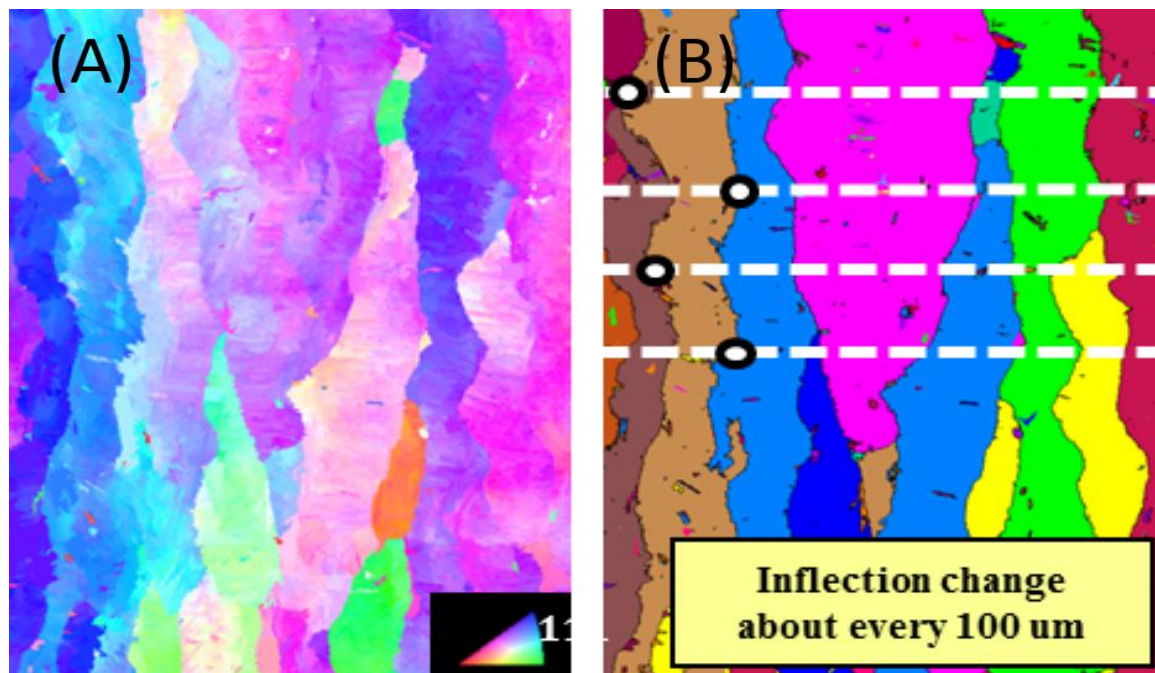


**Figure 13.** (A) EBSD scan of the LED sample perpendicular to build direction showing columnar features and (B) Prior beta grain reconstruction with annotations showing the serrated growth at roughly 30° to the build direction and inflections at multiples of the layer thickness (50µm), which is associated with the rotation strategy of the printing system.

## 7. Concluding Remarks

The printing process of metallic additively manufactured components is complex and leads to heterogeneous local processing conditions for the same global printing parameters. The geometry of individual samples, as well as their collective arrangement within the build domain, influences the processing history they will experience. This work shows that processing history affects defect and microstructure morphology, as well as crystallography. We have developed a simple yet effective model for determining spatio-temporal thermal histories within the build volume, and have shown that the histories correlate with observed microstructures. This model can be used to pre-calculate local processing conditions if the scan strategy of the system is known *a priori*. Potentially, this model could also be used to modify the build layout if it was desirable to homogenize thermal history.

## References

- [1] Hsieh J, Nett B, Yu Z, Sauer K, Thibault J-B and Bouman C A 2013 Recent Advances in CT Image Reconstruction. *Current Radiology Reports*
- [2] Wilkinson A J and Hirsch P B. Electron diffraction based techniques in scanning electron microscopy of bulk materials. *Micron*, **28**(4) 279
- [3] Besl P J and McKay N D. 1992 A method for registration of 3-D shapes. *IEEE Transactions on Pattern Analysis and Machine Intelligence*, **14**(2) 239
- [4] Rusu R B and Cousins S 2011 3D is here: Point Cloud Library (PCL). *IEEE International Conference on Robotics and Automation (ICRA)*
- [5] Lehmann G. 2006 Robust Automatic Threshold Selection. *The Insight Journal*
- [6] Zhong X, Rowenhorst D J, Beladi H and Rohrer G S 2017 The five-parameter grain boundary curvature distribution in an austenitic and ferritic steel. *Acta Materialia*, **123** 136
- [7] Barbe C B, Dobkin D P, and Huhdanpaa H T 1996 The Quickhull algorithm for convex hulls. *ACM Transactions on Mathematical Software*, **22**(4) 4693
- [8] Rosenthal D. The theory of moving sources of heat and its application to metal treatments. ASME, 1946.

- [9] Eagar T W and Tsai N S 1983 Temperature-Fields Produced by Traveling Distributed Heat- Sources. *Welding Journal*, **62**(12) S346
- [10] Nguyen N T, Ohta A, Matsuoka K, Suzuki N, and Maeda Y 1999 Analytical solutions for transient temperature of semi-infinite body subjected to 3-D moving heat sources. *Welding Journal*, **78**(8) 265S
- [11] Nguyen N T, Mai Y W, Simpson S and Ohta A 2004 Analytical approximate solution for double ellipsoidal heat source in finite thick plate. *Welding Journal*, **83**(3) 82S
- [12] Elsen M V, Baelmans M, Mercelis P, and Kruth J P 2007 Solutions for modelling moving heat sources in a semi-infinite medium and applications to laser material processing. *International Journal of Heat and Mass Transfer*, **50** 4872
- [13] Winczek J. Analytical solution to transient temperature field in a half-infinite body caused by moving volumetric heat source 2010. *International Journal of Heat and Mass Transfer*, **53**(25- 26) 5774
- [14] Khairalluh S, Anderson A T, Rubenchik A and King W E 2016 Laser powder-bed fusion additive manufacturing: Physics of complex melt flow and formation mechanisms of pores, spatter, and denudation zones. *Acta Materialia*, **108** 36.